Experimental Insights into the Coupling of Methane Combustion and Steam Reforming in a Catalytic Plate Reactor in Transient Mode

# Experimental insights into the coupling of methane combustion and steam reforming in a catalytic plate reactor in transient mode

M. Arsalan Ashraf[a,d,*,1], Stefano Tacchino[a], Nageswara Rao Peela[b,c], Giuliana Ercolino[a], Kirandeep K. Gill[d], Dionisios G. Vlachos[b], Stefania Specchia[a,*]

[a] Department of Applied Science and Technology, Politecnico di Torino, Torino 10129, Italy

[b] Department of Chemical and Biomolecular Engineering, University of Delaware-Newark, DE 19716-3110, USA

[c] Department of Chemical Engineering, Indian Institute of Technology, Guwahati 781039, India

[d] Department of Chemical Engineering, University of Bath, Bath, BA2 7AY, United Kingdom

* Corresponding authors. E-mail: muhammad.ashraf@polito.it (M.A. Ashraf)
stefania.specchia@polito.it (S. Specchia)

**Abstract**

The micro-structured reactor concept is very promising technology to develop a compact reformer for distributed hydrogen generation. In this work, a catalytic plate reactor (CPR) is developed and investigated for coupling of methane combustion (MC) and methane steam reforming (MSR) over $Pt/Al_2O_3$ coated microchannels in co-current and counter-current modes in transient experiments during start-up. A three dimensional (3D) computational fluid dynamics (CFD) simulation shows uniform velocity and pressure distribution profiles in microchannels. For channel velocity of 5.1 to 57.3 m/s in the combustor, the oxidation of methane is complete and self-sustainable without explosion, blow-off or extinction, nevertheless flashbacks are observed in counter current mode. In the reformer, the maximum methane conversion is 84.9% in the co-current mode slightly higher than that of 80.2% in counter-current mode at residence time of 33 ms, but at the cost of three times higher energy input in the combustor operating at ~1000 °C. Nitric oxide (NO) is not identified in combustion products but nitrous oxide ($N_2O$) is a function of coupling mode and forms significantly in co-current mode. This research would be helpful to establish the start-up strategy and environmental impact of compact reformers at small scale.

*Keywords:*
Catalytic plate reactor
Methane steam reforming
Methane combustion
Co-current mode
Counter-current mode

[1] Current affiliation of M. Arsalan Ashraf: "Dyson Technology Ltd, Tetbury Hill, Malmesbury SN160RP United Kingdom".

## 1. Introduction

Hydrogen is a zero carbon energy carrier for deployment of fuel cell technologies in distributed energy systems and offers great potential in transition towards a low-carbon economy. In addition to improved energy efficiency, hydrogen fuel cells can improve air quality with negligible emission of harmful particulates and nitrogen oxides. Hydrogen can be produced from a variety of feedstocks, such as non-renewable resources (i.e., natural gas, liquid fuels, coal, and so on) and renewable resources (i.e., biogas, biomass, solar, wind, hydropower, and so on) using electrolysis and reforming processes.[1, 2] Methane is the principal component of large distributed renewable (e.g., bio-methane, biogas) and non-renewable (e.g., natural gas, shale gas) feedstocks.[3] Despite of its significant advantages, the penetration of hydrogen in existing energy distribution network is very slow[4] and the lacking of hydrogen infrastructure is a key barrier for widespread application of fuel cell technologies, representing a typical chicken-and-egg problem. During the transition period, the distributed generation of hydrogen can be considered as a viable alternative via electrolysis and reforming technologies.[5]

The established reforming processes for low-carbon hydrogen generation are steam reforming, oxidative steam reforming, partial oxidation and autothermal reforming. Methane steam reforming (MSR) is a mature technology, dominant at industrial scale supplying 40% of world's hydrogen, with benefits of higher hydrogen yield and concentration in product stream as compared to other reforming technologies.[6-9] Conventionally, MSR is a highly endothermic reaction (Eq. 1) producing hydrogen and carbon monoxide. In the same reaction environment, the exothermic water-gas shift reaction (Eq. 2) transforms carbon monoxide into hydrogen and carbon dioxide in the presence of steam. MSR is carried out at industrial scale over Ni-based pellet catalyst packed in multi-tubular reformers operating at high temperature (>800 °C) and pressure (20 – 40 bar) with steam to carbon (S/C) molar ratio of 2 – 4.[10]

$$CH_4 + H_2O \leftrightarrow CO + 3H_2 \qquad \Delta H^o_{298} = +206.1\ \text{kJ/mol} \qquad (1)$$

$$CO + H_2O \leftrightarrow CO_2 + H_2 \qquad \Delta H^o_{298} = -41\ \text{kJ/mol} \qquad (2)$$

Heat transfer is critical for the steam reformer's design and performance. Energy is transferred from an external source[11] such as homogeneous or catalytic combustion (Eq. 3). Design of CPR requires the balance between heat input and heat consumption.[12] Significant research efforts have been devoted to achieving better temperature control of the reformer and proper handling of heat to enhance energy efficiency.[13-16] In a burner-fired industrial reformer, the heat is supplied mostly via radiative and convective transfer from combustion flames at >1400 °C to the walls of catalyst tubes and via conductive transfer from walls to the catalyst pellets in the tubes. The homogenous combustion in industrial burner releases significant amount of harmful pollutants such as carbon monoxide, nitrogen oxides and hydrocarbons. The nitrogen oxides in hot flue gases are 90 – 95% nitric oxide (NO) and the remainder 5 – 10% are nitrogen dioxide ($NO_2$) and

nitrous oxide ($N_2O$). The catalytic methane combustion (MC) is pursued for stable heat generation because a stable gas-phase combustion cannot be sustained below 1000 °C [17] above which thermal NOx forms[18, 19] and is a function of temperature, oxygen concentration and residence time.[20] The NOx and especially $N_2O$ emissions have not received attentions to date and are less defined in smaller power generation devices as compared to industrial plants,[21] especially in transient mode of start-up and shutdown.[22] A key issue in the design and thermal management of catalytic combustor is finding the operating regime for stable combustion.[23] Based on process requirement, the operating temperature for catalytic methane combustor can be categorized into low (300 – 700 °C) and high (700 – 1400 °C).[24] MSR is highly endothermic reaction requiring large amount of heat at temperatures up to 1000 °C [25] for attractive equilibrium conversion[26], which makes high temperature catalytic combustor as desirable.

$$CH_4 + 2O_2 \leftrightarrow CO_2 + 2H_2O \qquad \Delta H^o_{298} = -802.7\ \text{kJ/mol} \qquad (3)$$

The scaled down version of the industrial reformer shows poor performance and responds slowly to throughput variation, mainly because of heat transfer limitations between the flame and the catalyst pellet, and also due to mass transfer limitations.[27, 28] Furthermore, flames quench at small scales and catalytic combustion is needed.[29] By improving transport limitations, microreactor technology provides unique opportunities to realize compact and modular steam reformers.[30-33] In a microreactor, the improved heat and mass transport rates lead to 1 – 3 times higher throughput of hydrogen.[34] Radical improvement in reforming performance can be achieved by replacing the external firing by direct heating or more augmented methods of heat supply.[12] In this perspective, the catalytic plate reactor (CPR) is a potential candidate integrating combustor with reformer providing necessary heat mostly via conductive transfer.[35] The design of CPR permits higher heat transfer rates due to the short conduction length of thin plate and also higher mass transfer rates because of short diffusion path in thin catalyst layer,[36] thus making it efficient and compact.[31] Several modelling studies[36-54] were performed to design and optimize the CPR that combines the MSR and MC reactions for various applications.

Despite significant advantages of CPR, there are certain design and operational challenges that need further investigation to build confidence for its practical implementation. The primary concern is thermal imbalance in CPR followed by the formation of hot spots and temperature spikes, thus leading to poor reactor performance. Moreover, understanding of dynamics and control characteristics are among the operational challenges of CPR that should be considered at an early design stage. CPR has faster dynamics, due to its compact size, and any disturbance in temperature can potentially be outstripped rapidly because of its very low overall heat transfer resistance.[55] Daily start-up/shutdown is one of the unique requirements of a compact reformer for distributed hydrogen production. It is challenging and critical for the reformer operation due to process uncertainty, for example, poor synchronization of heat fluxes can result in

appearance of temperature peaks or extinction of combustion.[56] The development of localized temperature extremes and thermally imbalanced CPR may challenge the reformer dynamic operation prior to reaching stable operating profiles. This is especially true during the start-up phase of operation which must be adapted for a specific reaction.[57] Design methodologies to properly align the heat production and heat consumption in CPR include the distributed feed design,[54, 56, 58] a hybrid (segmented and continuous) catalyst coating,[38, 40, 41, 47, 59-61] a confined layer of phase change material as heat sink,[62] and bimetallic strips forming a thermally activated valve in combustion channels.[63]

The flow (co-current or counter-current) modes have a direct impact on the temperature profile and thermal behaviour of CPR[64] and may impact the reactor performance. Few experimental studies have been attempted for thermal coupling of MSR and MC in a CPR. Tonkovich et al.[65] investigated a microchannel methane steam reformer with integrated methane partial oxidation to produce syngas mixture for subsequent combustion. The reactor achieves methane conversion of >90% on reforming side at 850 °C and forms low amounts of NOx (< 10 ppm) on combustion side. Venkataraman et al.[31] reported self-sustained steady state operation of two-pass CPR in co-current mode at 800 – 1000 °C with methane conversion of 95% on the reforming side and >90% on the combustion side. In another study, Irankhah et al.[66] investigated the performance of methane compact reformer integrated with catalytic methane combustor under various operating conditions. As per author's knowledge, there is a lack of experimental study on thermal coupling of methane combustor and methane steam reformer in CPR in transient mode during start-up. In the present work, a catalytic plate reactor is developed with an integrated reformer and combustor and experiments are performed to couple methane steam reforming and combustion over 5wt%Pt/$Al_2O_3$ coated microchannels on alternate sides of a plate in co-current and counter-current flow modes.

## 2 Materials and methods

### 2.1 Catalytic plate reactor

The CPR is developed to allow combustion and reforming streams to flow in the same direction on alternate side of the middle plate for co-current mode and in opposite direction for counter-current mode. The flow area of CPR is comprised an inlet distributor, 10 rectangular shaped microchannels and an outlet collector (Figure 1), and the design is based on the criteria described in the study by Commenge et al.[67]

The CPR is fabricated of 304 stainless steel with assembly of two side-plates and one middle-plate and two microchannel-plates, as shown in Figure 1a. The overall geometrical dimensions of the assembled CPR are 108 mm (length), 75 mm (width) and 15 mm (height), as shown in Figure 1b, where middle-plate is sandwiched in between two side-plates and each side-plate has inlet and outlet tubes. The microchannel plate (50 mm × 20 mm × 1 mm) is fabricated with 10 engraved parallel rectangular shaped microchannels

(50 mm × 1 mm × 0.5 mm). In the study by Zanfir et al.,[36] a decrease in channel height (0.5 – 2 mm) at constant flow rate does not introduce significant difference in reactors performance but a slight improvement in outlet conversion is observed due to reduced external mass transfer coefficient. The two side-plates have same dimensions and are engraved with rectangular housing for stainless steel reinforced graphite gaskets to avoid gas leakage. The housing is engraved on both sides of middle-plate for removable microchannel plates along-with inlet distributor and outlet collector. The collector and distributor are designed to ensure uniform flow through microchannels, and also serve as feed preheater.

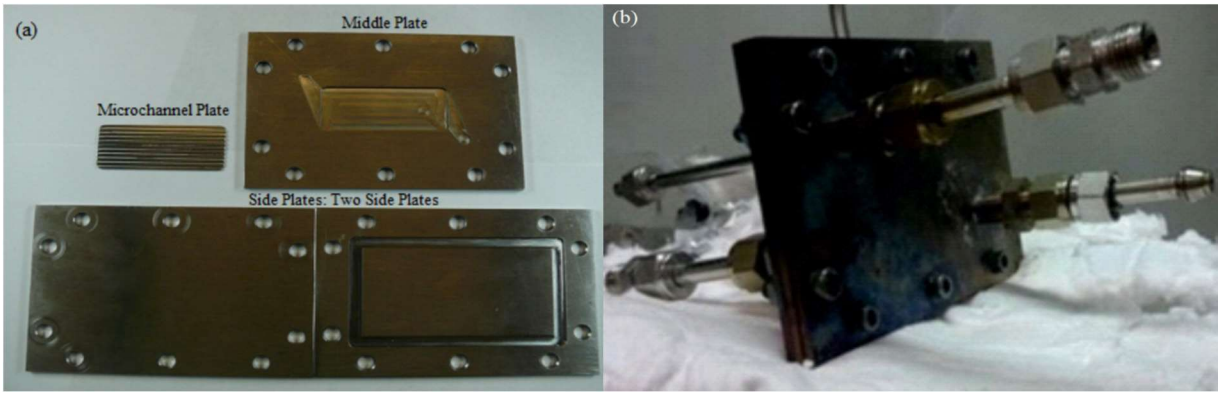


Figure 1. Images of catalytic plate reactor: (a) components of CPR, (b) assembled CPR

A 3D CFD model is employed in COMSOL Multiphysics to investigate flow uniformity and distribution, under the range of experimental flow rates, in microchannels (Figure 2) prior to reactor fabrication. The free and porous media flow interface is applied and governed by the continuity (Eq. 4) and Navier-Stokes (Eq. 5) equations representing mass and momentum balance, respectively, and solved using the finite element method.

$$\nabla(\rho \cdot u) = 0 \tag{4}$$

$$\rho(u \cdot \nabla)u = \nabla \cdot [-pl + \mu(\nabla u + (\nabla u)^T] \tag{5}$$

where $\rho$ is fluid density, $u$ is velocity, $p$ is pressure, and $\mu$ is fluid dynamic viscosity. This is applicable to isothermal and incompressible fluids under the condition of negligible gravitational forces. Nitrogen is considered as the model fluid flowing at 20 °C and reactor outlet pressure of 1 atm. The free tetrahedral mesh is selected with a mesh size of 0.2 mm, balanced between computational time and accuracy, to produce approximately 600,000 elements. The GMRES (generalized minimum residual) iterative linear solver is applied with left preconditioning. Pre- and post- smoothing are carried out using the Vanka algorithm and the convergence is achieved when the solution residuals reached $10^{-4}$ or below with relative tolerance set to 0.001.

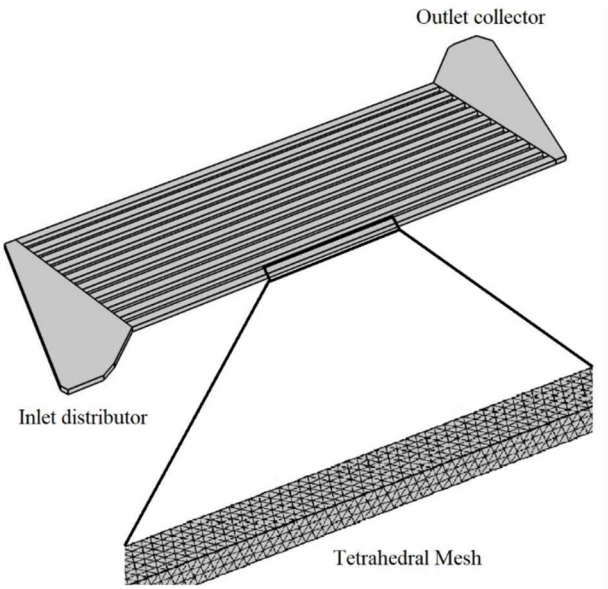


Figure 2. Microreactor: inlet flow area, distributor, 10 microchannels and outlet flow area.

## 2.2 Catalyst preparation and characterization

The commercial Ni-based catalyst for compact reforming[50, 68] is somewhat limited due to its susceptibility to deactivation and inability to effectively rapidly remove the heat of combustion, resulting in high temperatures and materials stability and safety issues, especially when exposed to daily startup shutdown. The wash coated precious metal catalyst permits a tenfold reduction in reactor size compared to Ni catalyst pellets. The relatively higher cost of noble metal catalyst is alleviated when considering the reduced reactor size and existing precious metals recycling processes.[69]

The noble metal based catalysts employed for MSR are Rh, Ru, Pt, and Ni, [70-72] and for MC are Pd, Pt, and Rh.[73, 74] The platinum catalyst is preferred in most cases and selected for this study due to its good activity toward both reactions. In a study, the effect of Pt catalyst loading (0.03 – 30 wt%) on γ-alumina was investigated for MC and a maximum methane oxidation rate was observed at 5 wt%.[75] The 5% Pt/$Al_2O_3$ catalyst layer is coated over microchannels by following the steps: (i) substrate pre-treatment, (ii) primer coating, (iii) slurry washcoating, and (iv) incipient wetness impregnation. The primer coating, slurry properties, and washcoating procedure strongly influence the adherence, uniformity, and the loading of catalyst layer over the aluminium-free stainless steel microchannels, as investigated in a previous study,[76] and the optimized conditions for washcoating of γ-$Al_2O_3$ on the microchannels were selected.

In the substrate pre-treatment, the surface of stainless steel microchannels is treated with aqua regia, a mixture of 1:3 molar ratio of nitric acid (70%, Sigma Aldrich) and hydrochloric acid (37%, Sigma-Aldrich), increasing surface roughness to help anchoring the primer layer. To remove any contamination, the microchannel-plates are cleaned with a soap solution followed by sonication in acetone-water solution at

33 kHz for 60 min. After washing with deionized water, the microchannel plates are finally dried at 120 ºC in stagnant air.

In the primer coating step, the microchannels are coated with a thin alumina primer layer to further enhance adherence of the alumina washcoat. A pimer solution (2% alumina, 4% polyvinyl alcohol) is prepared using a boehmite sol and polyvinyl alcohol (PVA, Sigma-Aldrich) in water. Boehmite sol is prepared by adding aluminium hydroxide (Disperal P2, 45μm, Sasol) to a 0.4wt% $HNO_3$ aqueous solution and then aged for 48 h to complete the peptization process. Boehmite sol is mixed with the required amount of PVA and stirred for 2 h. PVA is used as a slurry stabilizer and an additive to control drying and reduce crack formation in the alumina layer. After filling the microchannels with the primer solution, the microplates are dried at room temperature for 3 h and at 120 ºC for 8 h, and then finally calcined in stagnant air at 600 ºC for 5 h.

In the washcoating step, the slurry (14 wt% γ-$Al_2O_3$, 2 wt% PVA, 3 wt% colloidal alumina) is washcoated over the primer coated microchannels. Colloidal alumina AL20 (20 wt% aluminium hydroxide oxide, NYCOL) is used as inorganic binder. A 30 wt% aqueous γ-$Al_2O_3$ (Fluka) slurry is milled in ball mill (Pulverisette 6, Fritsch, Germany) and the pH is adjusted to 3.0 by adding nitric acid. After adding the required amounts of PVA and colloidal alumina, the slurry is stirred for 2 h and left for 24 h at ambient conditions. A coating of alumina washcoat is applied by filling the primer-coated microchannels with alumina-slurry. Then the microchannels are dried at room temperature for 3 h and at 120 ºC for 8 h, and then calcined in stagnant air at 600 ºC for 5 h. The washcoat layer outside the channel is removed and the washcoating process is repeated until the desired weight is obtained.

In the incipient wetness impregnation step, the Pt (5 wt%) catalyst is impregnated onto the alumina washcoated microchannels. The aqueous solution of tetra-ammine platinum (II) nitrate ($[Pt(NH_3)_4](NO_3)_2$, 99.995% trace metal basis, Sigma-Aldrich) is added dropwise with a micro-pipette on alumina washcoat in the microchannels. The catalytic microchannel plates are dried at 120 °C for 10 h followed by calcination in stagnant air at 300 °C for 2 h.

The topology of uncoated, acid treated and washcoated microchannels is examined using scanning electron microscopy (SEM FEI Quanta Inspect LV 30 KV). The adherence of catalyst layer to microchannels is very important for successful application of the microreactor. The adherence of catalyst layer is evaluated using ultra-sonication. The washcoated microplates are dipped in acetone and water solution (50:50 vol%) in a glass beaker and sonicated at 33 kHz and 130 W for 30 min in the S3M 2200 device by Sonica. Then the microchannel plates are dried at 110 ºC for 30 min and the procedure is repeated. The percent weight loss ($\Delta W$) is the normalized weight difference of microplates before ($W_b$) and after ($W_b$) the ultrasonic treatment, as described by the following equation.

208 $$\Delta W(\%) = \frac{(W_b - W_a)}{W_b} \times 100 \quad (6)$$

209 **2.3 Experimental setup**

210 A schematic diagram of the experimental setup is depicted in Figure 3. It is comprised a feeding system,
211 a catalytic plate reactor, and an analysis system. The gases (i.e., methane, air and nitrogen) are supplied
212 from high pressure cylinders using Brooks mass flow controllers, then premixed at desired flow rates and
213 fed to the CPR operating at atmospheric pressure. The flow rate of deionized water from a $N_2$-pressurized
214 water vessel is controlled by a Bronkhorst mass flow controller. The feed water is evaporated and mixed
215 with methane at 120 °C in a specially designed evaporator-mixer. The reformer feed tube is wrapped with
216 electric trace heating and maintained at temperature >120 °C to avoid water condensation. The combustor
217 feed tube is not heated externally by electric trace heating.

218 The CPR is placed in a horizontal split tube furnace (Carbolite, 500 mm heating length) with a PID
219 temperature regulator. To minimize heat losses, the CPR is insulated with vermiculite (3M Italia S.p.A)
220 and aerogel (Aspen Aerogels). The feed tubes (24 cm each) inside the furnace serve as preheaters before
221 entering the CPR. It is important to confine the combustion reaction in the combustion channels, and for
222 this purpose, the inlet and outlet tube of the combustion section are filled with alumina balls to suppress
223 the propagation of flames. It is difficult to insert a thermocouple in the reaction channels; therefore, two K-
224 type thermocouples are mounted at the outer surfaces of CPR to measure the combustion ($T_{COMB}$) and
225 reforming ($T_{REF}$) surface temperature. To record the furnace temperature ($T_{FURN}$), a third K-type
226 thermocouple is positioned in the wrapped insulation at a distance of 5 cm from the CPR inside the furnace.

227 The effluent product streams from the reformer and the combustor are passed through water condensers
228 before feeding to online gas analysers. The dry reformed gas is analysed by a non-dispersive infrared
229 absorption analyser (NDIR Uras 14 for $CH_4$/CO/$CO_2$, ABB Company) and a thermal conductivity analyser
230 (Caldos 17 for $H_2$, ABB Company). The composition of the combustion outlet stream is measured by a
231 paramagnetic analyser (MAGNOS 106 for oxygen) and a non-dispersive infrared analyser (URAS 14 for
232 CO/$CO_2$/NO/$N_2O$/$CH_4$, ABB Company).

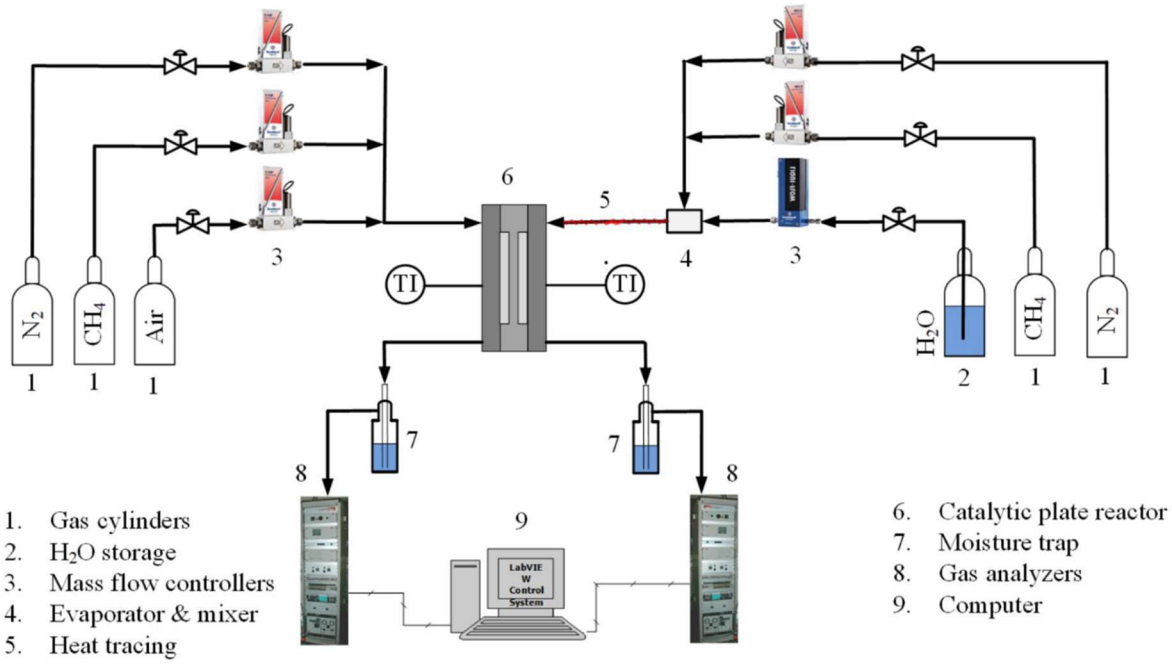


Figure 3. Schematic of experimental setup for coupling of MSR and MC in catalytic plate reactor.

The main challenge for methane combustor is to raise its temperature to ignition point, which can be achieved by resistive heating or using a self-igniting fuel-catalyst system. This methodology is also applicable to a CPR stack comprising of multiple plates. Zhang et al,[77] used an electrically resistive heated catalyst to ignite MC while coupling with MSR in the alternate channels of the CPR. To initiate CPR heating at room temperature, hydrogen is a promising candidate that can be ignited over Pt catalyst but results in non-uniform temperature profile and poses an explosion risk.[78] On the other hand, part of the methane reforming feed can be used in combustor but requires a high temperature to initiate the oxidation reaction.[66] In the present study, an electric furnace is used for heating the reactor to the desired reaction temperature. Initially heat from electric furnace is used to initiate methane combustion and after that the methane-air flow in combustor is varied to regulate the reactor temperature.

Prior to coupling experiments, preliminary experiments are carried out in CPR to evaluate the activity of 5% $Pt/Al_2O_3$ towards MC and MSR reactions. The reactor is placed without insulation in the electric furnace to provide heat necessary for the reaction. The feed stream is passed through one side and nitrogen (100 mL/min) on the other side of the reactor. Nitrogen flow of 100 mL/min is passed through the reactor during cooling to avoid catalyst damage.

In each coupling experiment, the start-up of the reactor is performed in two phases: i) a furnace-heating phase and ii) a furnace-off phase. In the furnace-heating phase, heat is provided from the electric furnace to initiate MC and increase the reactor temperature at a ramp rate of 10 °C/min. Prior to start heating, the reactor is purged with $N_2$ at a flow rate of 100 mL/min for 30 minutes. Then methane and air streams are

premixed and replace the nitrogen stream. Meanwhile on the reforming side, nitrogen flow is switched to a constant methane-steam mixture flow when $T_{ref}$ reaches 400 °C. One important factor to consider during start-up is the susceptible formation of carbon deposits on the catalyst surface in the reformer.[79] Therefore to avoid coke formation, MSR is performed at a steam to carbon molar ratio (S/C) of 4 that is very close to the typical industrial reforming value of 3.3, much higher than the minimum ratio of 1.7.[36] In the second furnace-off phase, $T_{COMB}$ was monitored, and methane-air flow rate was varied manually to control the amount of energy on the combustion side to regulate the reactor temperature. The reactor temperature is raised to a maximum of 1100 °C for a short duration without detection of any visible physical deterioration. For safety and to avoid catalyst deterioration, the reactor is purged with nitrogen (100 mL/min) during cooling. The methane conversion ($X_{CH_4}$) and CO selectivity ($S_{CO}$) are defined as follows:

$$X_{CH_4} = \frac{F_{CH_4.in} - F_{CH_4,out}}{F_{CH_4.in}} \times 100 \quad (7)$$

$$S_{CO} = \frac{F_{CO\ out}}{F_{CH_{4,in}} - F_{CH_{4,out}}} \times 100 \quad (8)$$

where $F_{CH_4}in$, $F_{CH_4}out$ are the inlet and outlet molar flow rates of methane and $F_{CO,out}$ is the outlet molar flow of carbon monoxide.

## 3. Results and discussion

### 3.1 CFD Modelling

The catalytic plate reformer needs careful design to avoid flow maldistribution, a typical pathology, for uniform reaction conditions in each channel and higher reforming efficiency in the reformer.[80] Any flow maldistribution can lead to burning more methane in one or more channels, misalignment of reaction zones, hot spot formation, overheating, and significantly lower reformer performance.[81, 82] A two-dimensional (2D) view of the velocity profile in the flow area of the CPR is shown in Figure 4 (a – c) for an average channel inlet velocity at 1.4 m/s, 32.2 m/s and 57.3 m/s, respectively. More data in terms of channel inlet velocity and velocity profiles are shown in Table S3 and Figure S1. The highest velocities occur at the inlet and outlet of the flow distributors. The difference between the highest and the lowest velocities in the microchannels is never higher than 7.1% of the average value. The difference between the minimum and maximum velocities in microchannels increases linearly with the average velocity, as shown in Figure S2. In spite of these variances, uniform velocity profiles are obtained across the microfluidic channels to enable high performance reactions.

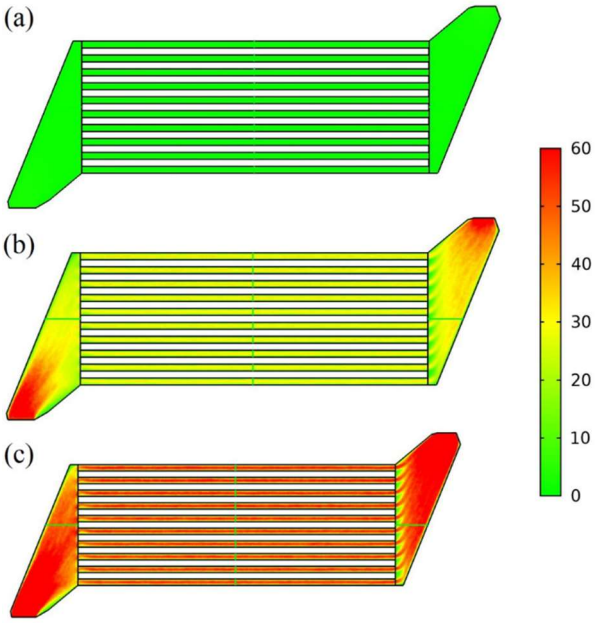


Figure 4. 2D velocity profile in flow area of CPR at average channel inlet velocity of (a) 1.4 m/s, (b) 32.2 m/s and (c) 57.3 m/s.

An additional approach to assess the flow is by investigating the pressure drop. The pressure profile in the flow area of CPR is shown in Figure 5 for channel inlet velocity from 1.4 to 57.3 m/s; the pressure is uniformly distributed across all the microchannels (see also Figure S3). The pressure drop contributes to parasitic losses and is important for practical application. The pressure drop across the micro channels is increased from 81 to 57397 Pa as the flow increases from 0.4 to 15.7 L/min, as shown in Table S4. Therefore, the maximum velocity is an important parameter to be controlled to remain within acceptable pressure drops. Unfortunately, there is a lack of experimental data to validate the pressure drop estimated from fluid flow model.

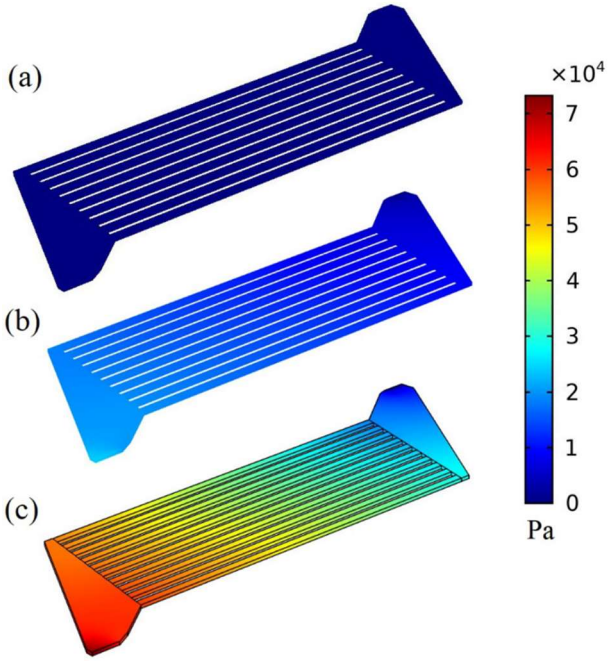


Figure 5. 3D pressure profile in the flow area of the CPR at a channel inlet velocity of (a) 1.4 m/s, (b) 32.2 m/s and (c) 57.3 m/s.

### 3.2 Catalyst Characterization

The surface roughness of stainless steel microchannels is analysed using SEM before and after the acid treatment, as shown in Figure 6 (a – b), respectively. The result shows an enhanced surface roughness after acid treatment (Figure 6b) which could amplify the adherence of the washcoat layer in the microchannels. The thickness of the primer layer is estimated as 1.46 µm considering the apparent coating density of 1.5 g/cm$^3$ and the primer layer weight gain.

The SEM image (Figure 6c) shows the morphology and homogeneity of Pt/$Al_2O_3$ catalyst layer coated on the walls of microchannels. The catalyst layer is homogeneous and uniformly distributed throughout the channel with strong washcoat-wall interaction. The catalyst layer shows a rough, porous, and uniform morphology. Minor cracks are observed in the catalyst layer which may be due to the stresses developed by shrinkage and gas formed during drying and calcination. The average catalyst layer thickness in the microchannels varies from 121 µm (10.2 mg/cm$^2$) to 147 µm (12.4 mg/cm$^2$). The higher catalyst loading offers performance advantages in dynamic mode of heat exchange-microreactor[83] but is quite a challenging to coat a thick catalyst layer on a metallic microchannel with good adherence.[84]

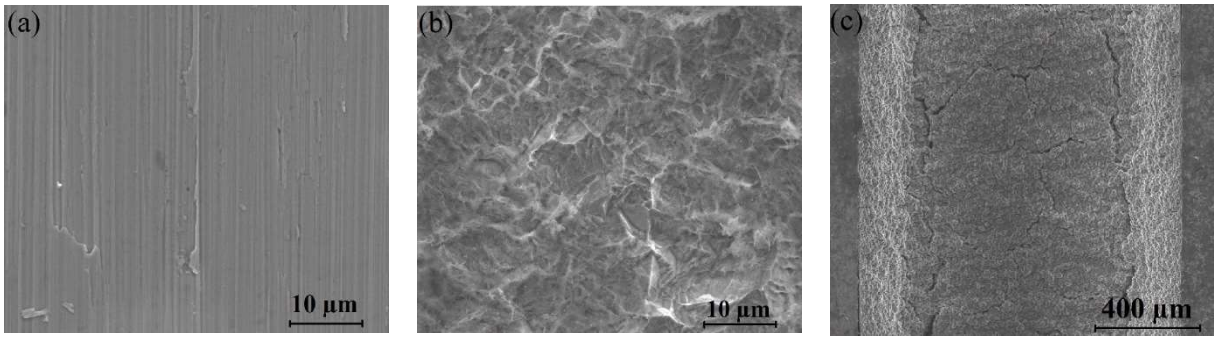


Figure 6. SEM images of topology of microchannels of (a) uncoated, (b) acid treated microchannel, and (c) catalyst coated.

The mechanical stability of catalytic washcoat lined over stainless steel microchannels is critical to avoid catalyst loss during operation. Quantification of the catalyst layer's adherence can be done by ultra-sonication, simulated environment, thermal shock, drop test, abrasive test, pull-off method and scratch methods.[85] For comparison with previous work,[76] the adherence of washcoat is evaluated by most commonly used ultra-sonication method and no peeling off of the catalyst layer was observed. The weight loss of two microplates is evaluated as 9.5% and 10.3% with an average value of 9.9% in good agreement with the prior work.[76] Weight loss of less than 12% represents good adherence that is necessary for successful application of catalyst coated microreactor.

### 3.3 Single reaction in the catalytic plate reactor (CPR)

#### 3.3.1 Catalytic methane combustion (MC)

MC is evaluated by varying the reactor temperature with premixed methane-air mixture (5 vol % $CH_4$ in air, equivalence ratio = 2) flowing over 5wt% $Pt/Al_2O_3$ coated microchannels at a constant residence time of 41.1 ms. The equivalence ratio ($\lambda$) is defined as the ratio of actual air-fuel ratio to the stoichiometric air-fuel ratio for a given mixture. Lean methane-air mixtures are favourable to achieve high conversion and thermal efficiencies as compared to a stoichiometric mixture.[86, 87] As shown in Figure 7, methane conversion starts at 0.3% at 400 °C, and increases to 98.1% at 900 °C. The temperatures ($T_{10}$, $T_{50}$, $T_{90}$) at which methane conversion reaches 10%, 50% and 90% are 589 °C, 669 °C and 845.5 °C, respectively. In a study for lean methane-air mixture ($\lambda = 2$),[88] methane conversion of 95.7% was obtained at 450 °C over 3.8wt% $Pt/Al_2O_3$ coated microchannels with a residence time of 14.4 s in a stainless steel microreactor. The exhaust fraction of $CO_2$ and CO was increased to 8.6% and 0.3%, respectively, at 900 °C. The notable CO formation above 800 °C might be due to the contribution of slow homogeneous combustion[89] which is unavoidable above 600 °C [25] or steam and dry methane reforming reactions during combustion.[90] The results may suggest the presence of both catalytic and homogeneous MC in the reactor, where the purely homogeneous gas-phase MC cannot be sustained in channels gap below a critical dimension of 2.8 mm for

premixed lean methane-air mixtures.[91] The coexistence of homogenous combustion in a catalytic combustor makes catalytic combustion more complex, which leads to complex coupling the two.[92] However, the catalyst still maintained its utility in limiting the formation of CO through its oxidation into $CO_2$.

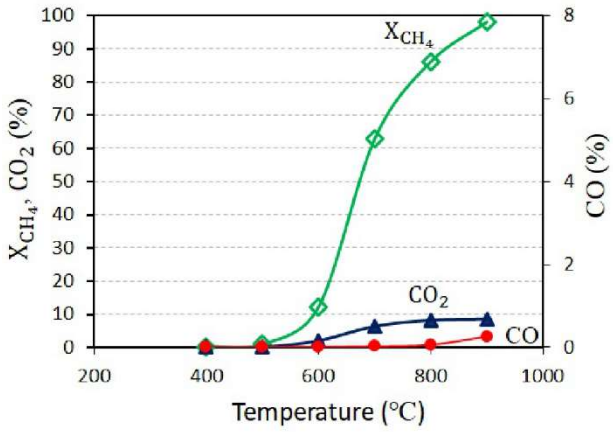


Figure 7. Methane conversion and product (CO and $CO_2$) composition as a function of temperature.

### 3.3.2 Methane steam reforming

Steady state MSR is carried out by varying reactor temperature over 5wt% $Pt/Al_2O_3$ coated microchannel at constant space velocity (WHSV = 36 NL/h/$g_{cat}$) with S/C ratio of 4.0. As shown in Figure 8a, methane conversion is increased with temperature as it reaches 73.4% at 900 °C and hydrogen concentration follows the same pattern with a value of 70% at 900 °C. Similar to CO concentration (Figure 8a), CO selectivity (Figure 8b) also increases from 25% to 47.9% with a rise in temperature. As a measure of the selectivity to hydrogen, the $H_2$/CO molar ratio shows an opposite trend to methane conversion and drops from 34.5 to 7.2, similar values were also observed in the previous studies,[70, 71] probably due to increased contribution of MSR over the water-gas shift reaction at higher temperatures. At lower temperatures, the high $H_2$/CO ratio is because of the lower methane conversion and the significant contribution of the water-gas shift reaction.

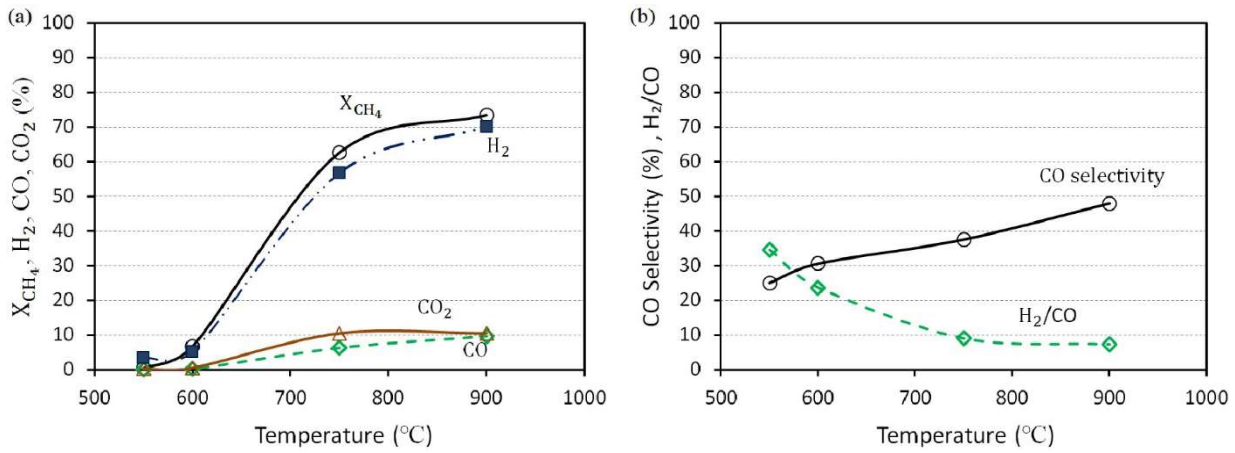


Figure 8. Steady state MSR performance as a function of temperature (a) methane conversion and product gas ($H_2$, CO, $CO_2$) composition and (b) CO selectivity and $H_2$/CO ratio.

### 3.4 Coupled reactions in the catalytic plate reactor (CPR)

For coupling experiments in co-current and counter-current modes, the reformer is operated at constant methane flow of 45 mL/min and S/C of 4:1 (WHSV of 110 NL/hr/$g_{cat}$, channel inlet velocity of 1.5 m/s, and residence time of 33 ms). After high methane conversion in the combustor is reached, the electric furnace is turned off and the heat generated is used to maintain $T_{COMB}$ at ~ 1000 °C by regulating the methane-air flow (7 vol% $CH_4$, stoichiometric ratio $\lambda = 1.40$). The autoignition temperature of gas-phase MC is minimum at 7 vol% methane in air and is 600 °C [93]. The heat generated in the form of thermal energy ($W_t$) is calculated based on the lower heating value of methane ($LHV_{CH_4}$). The combustor feed channel inlet velocity of 5.3 – 60.9 m/s (residence time of 9.5 – 0.8 ms) is much higher than the typical channel inlet velocity of 1 m/s in a micro-combustor.[23] For co-current and counter-current operation, the combustor channel inlet velocity as a function of time on stream is provided in Supplementary Information (Figure S4). Freshly coated catalytic microchannel plates were used for each experiment and no deterioration of catalyst layer was observed after each experiments. The expansion and contraction during start-up and shutdown and associated attrition are alleviated by having the noble metal catalyst washcoated on metallic structures.[94]

The internal and external mass transfer limitations are evaluated for MSR at the maximum conversion in the co-current and counter-current modes. The absence of external mass transfer limitation in MSR reaction is confirmed using the Carberry criterion[95] (co-current mode: 0.007< 0.05, counter-current mode: 0.006 < 0.05), see Supporting Information. The reactants diffuse from the alumina washcoat surface through the pores to the Pt catalyst active sites. The lack of significant diffusion limitation in the catalyst washcoat is established using the Weisz-Prater criterion[96] (co-current: 0.91 < 1.0, counter-current: 0.85 < 1.0).

### 3.4.1 Co-current coupling

In co-current mode, the feed streams flow in the same direction in the combustor and reformer on alternate sides of the middle plate. In the combustor, the methane conversion increases with time, as shown in Figure 9. The temperatures ($T_{10}, T_{50}, T_{90}$) of the combustion surface at which MC reaches conversion of 10, 50, and 90% are 631, 861, and 884 °C, respectively. Complete methane conversion is achieved at $T_{comb}$ of 901 °C and TOS of 50.2 min. In an experimental study, Ismagilov et al.,[97] observed the ignition temperature of 1037 °C for MC over $Pt/Al_2O_3$ catalytic foam while coupling with MSR in a catalytic heat exchange-tubular reactor. The concentrations of $CO_2$ and CO increase with methane conversion and reach values of 10.6 vol% and 0.65 vol% (6460 ppm), respectively, at 901 °C. Both catalytic reactions as well as homogeneous gas-phase reactions may contribute to CO formation. As the reactor temperature increases, gradient in temperature between the catalyst surface and bulk gas in the microchannels may form, which may initiate gas-phase combustion in the boundary layer. With further rise in temperature, reactions may start in the bulk phase and their rate can significant.[18] For MC, homogenous gas-phase reactions start contributing at >700 °C.[24] In transient and steady state operations, gas-phase reactions result in reduced $CH_4$ emissions and increased CO emissions.[23] After complete methane conversion, CO declines sharply down to 25 ppm that confirms the contribution of catalytic reaction in MC. After a stabilizing period of about 14 min, the CO concentration jumps up to 586 ppm and the $CO_2$ concentration declines down to 9.6 vol% at 64 min when the thermal energy input was increased to 112 $W_t$. At this point gas-phase temperature in the microchannel might have reached a value where homogeneous reaction starts contributing more. A downward spike in methane conversion is also observed with a quick recovery at each flow variation due to time needed for the system to re-equilibrate.

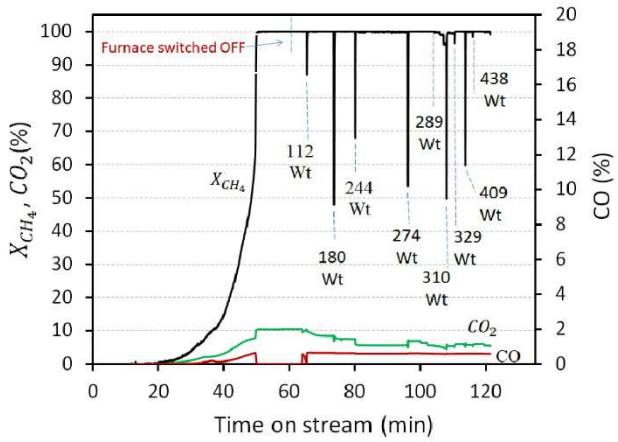


Figure 9. Methane conversion and concentration profiles in the combustion side in co-current operation as a function of time on stream.

After stabilization of the MC reaction, confirmed by product gas composition online analysis, the furnace is switched off at $T_{FURN}$ of 1021 °C and heat from the combustor sustains both the oxidation reaction[90] and steam reforming reaction. The principal method of heat transfer is wall-to-wall/in-wall thermal conduction. However, the heat transfer by radiation become significant as the wall temperature exceeds 800 °C.[18] In the absence of sharp temperature peaks in Figure 10, $T_{COMB}$ profile indicates that the MC is stabilized and confined inside the catalytic microchannels. After turning off the electric furnace, $T_{FURN}$ is drops continuously and $T_{REF}$ and $T_{COMB}$ differ somewhat. As the furnace temperature drops below the reactor temperatures, the thermal energy input is increased exponentially (Figure S5) to compensate for the heat losses to maintain $T_{COMB}$. For example, when set at 438 $W_t$, $\Delta T_1 = T_{COMB} - T_{FURN} = 295.7\ °C$ and $\Delta T_2 = T_{COMB} - T_{REF} = 54.1\ °C$ at the end of experiment.

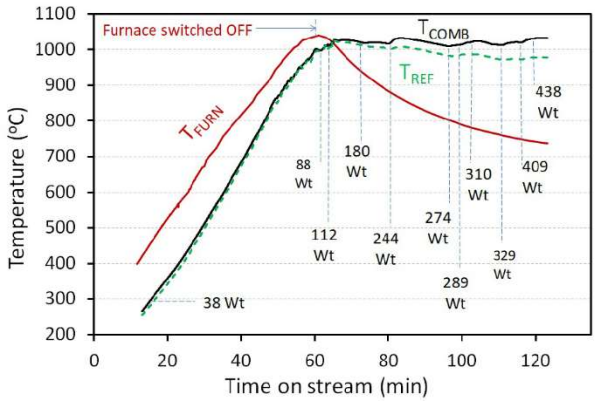


Figure 10. Temperature profile of co-current mode in CPR.

NO is not detected in the combustor outlet thus excluding thermal NO formation known as the Zeldovich mechanism.[98] The use of a lean methane-air mixture also excludes fuel rich (prompt NO) and fuel bound NO mechanisms. Another route for NO formation is by oxidation of $N_2O$ intermediate to NO through the $N_2O$ mechanism during lean MC when the combustion temperature is below 1200 °C.[99-101]. By this mechanism, $N_2O$ formation is initiated by recombination of molecular nitrogen with atomic oxygen by a three-body recombination reaction ($O + N_2 + M \rightarrow N_2O + M$), where M is any collision partner, followed by oxidation of $N_2O$ to NO.[102] The formation of $N_2O$ is confirmed at $T_{COMB}$ of 490 °C, as shown in Figure 11. $N_2O$ formation becomes important at gas phase temperature of > 550 °C, well within the range of catalytic combustion.[90] Formation of significant quantities of $N_2O$ can occur by catalytic reactions.[18, 103] The appearance of $N_2O$ only in the product stream suggests that the residence or the temperature is not high enough for the decomposition of $N_2O$ to NO. With increase in energy input, the $N_2O$ level rises sharply till 580 ppm then it is incremental to > 650 ppm, which is much higher than the

$N_2O$ concentration of <5 ppm found in most combustion devices. The main exception to this is fluidized bed which burns coal forming flue gas with $N_2O$ ~50 ppm.[104]

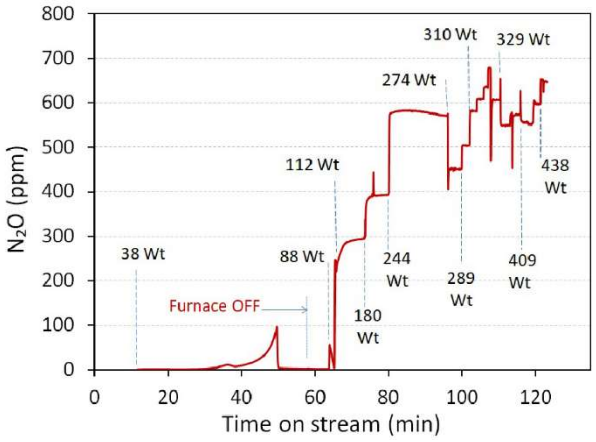


Figure 11. The concentration of $N_2O$ (ppm) for co-current mode in catalytic plate reactor.

In co-current flow, the temperature is the highest near the channel inlet of the methane combustor and the kinetics of reforming is also very fast. Due to early conversion in channels[46] and overlapping of reaction zones in co-current mode, the heat generated by MC is subsequently used by the endothermic steam reforming reaction on alternate side of the middle plate. Overlap of reaction zones helps to reduce hot spots and temperature spikes.[105] Co-current flow mode is favourable in preventing the runaway of highly exothermic reactions where cooling is provided by steam reforming. The combustion generates surplus heat which is consumed by the highly endothermic steam reforming reaction moving in the same direction on alternate side due to overlapping of both reaction zones. This overlapping of reaction zones helps to reduce hot spots in the reactor.[105]

The methane conversion, CO selectivity and $H_2$ fraction increase with reactor temperature during the furnace heating phase, as shown in Figure 12. The highest $CH_4$ conversion (84.9%) $H_2$ fraction of 68.1% occur at $T_{REF}$ of 1022 °C when the temperature difference between $T_{FURN}$, $T_{COMB}$ and $T_{REF}$ is at minimal. The corresponding CO selectivity is 61.3% and continues to rise and stabilizes at ~ 70% when the combustion surface temperature is maintained at ~1000 °C. As per the study of Zanfir et al.,[36] the catalyst layer thickness has a pronounced effect on the thermal behaviour and outlet conversions and the drop in reforming performance at higher catalyst loading is more pronounced compared to catalytic combustion. The drop in $CH_4$ conversion can be attributed to heat losses resulting from the colder environment once the furnace is turned off. This comes with concomitant decrease in hydrogen concentration and a more gradual decrease in CO. Good performance of the reactor requires fast heat exchange between the two sides and low heat dissipation to the surroundings. The high heat loss results in significant loss of efficiency.[51]

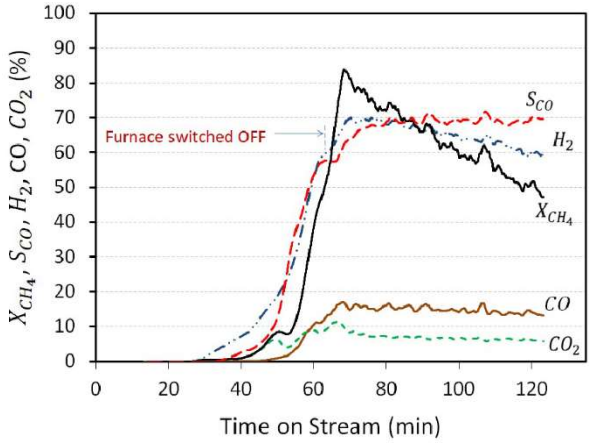


Figure 12. $CH_4$ conversion, CO selectivity and percent profiles ($H_2$, CO and $CO_2$) of MSR for co-current flow mode with methane flow rate of 45 mL/min and S/C molar ratio of 4.0.

Another experiment was performed with fixed flows to combustor and reformer in the CPR to further investigate the effect of heat loss on MSR during co-current operation. After complete methane combustion was achieved, the furnace was turned ON and OFF, to estimate the heat necessary to overcome external heat losses and maintain the reactor temperature. The results are provided in the Supporting Information (Figure S6 – S9). The methane conversion with the furnace on was stabilized at 35 ± 4% but dropped under heat loss. A similar influence of heat loss on the reformer performance was observed during coupling of MSR and MC in a previous study,[51] where the methane conversion in the steam reformer dropped from 80% under adiabatic conditions to 10% under laboratory heat loss conditions. As mentioned in the study of Mettler et al.,[48] methane fuelled smaller microreactor stacks are unstable because of heat losses. Moreover Mettler et al.,[51] also investigated the influence of number of catalytic plates in stack reactor on the coupling of exothermic and endothermic reactions for syngas production. The results suggest that the heat losses strongly influence the combustion reaction and the energy transfer from combustion to reforming side declines and decrease the performance of the reformer. The negative influence of heat losses can be minimized by increasing the number of catalytic plates in stack reactor. Under laboratory heat loss conditions, the moderately conductive walls of stainless-steel catalytic plate reactor are unstable due to lack of effective insulation. As suggested by Mettler et al.,[48] the stability of plate reactor can be enhanced by increasing the number of catalytic plates, enhancing the net power input, modifying the dimension and wall material, increasing catalyst loading, and changing combustion fuel. As per theoretical study by Zanfir and Gavriilidis,[53] co-current is more thermally balanced and shows lower conversion for MSR as compared to counter-current operation.

### 3.4.2 Counter-current coupling

For counter-current mode, the temperature profiles of CPR are shown in Figure 13. The temperatures ($T_{10}, T_{50}$, and $T_{90}$) to reach 10, 50, and 90% methane conversion in the combustor are 754, 920, and 934 °C, respectively. Complete conversion for methane is observed at $T_{COMB}$ = 943 °C, $T_{FURN}$ = 1038 °C and $T_{REF}$ = 924 °C.

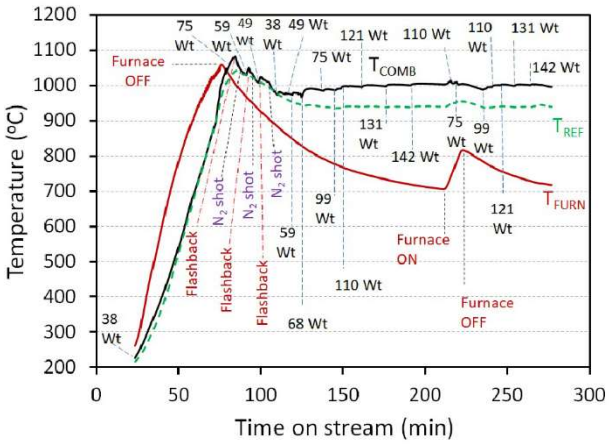


Figure 13. Temperature profile in counter current flow operation.

The MC reaction becomes thermally unstable due to either flashback, in which the reaction front propagates upstream, blow-off, in which reaction front propagates downstream, or extinction [87]. After switching-off the furnace at $T_{FURN}$ of 1059 °C, three flashbacks are observed in the combustor when the flame velocity exceeds the methane-air mixture inlet velocity.[106] The flashbacks appear after three excessive temperature peaks with a sharp decline in $T_{COMB}$ profile and the flame moves from the catalytic channels to the feed tube just after the alumina ball packed flame arrestor. These high temperature peaks are a main obstacle in the implementation of counter-current operation mode.[107] The delocalization of reactions zones leads to extra heat generation that drives the combustion temperature to be unnecessarily high resulting in flashback. After each flashback, the combustor is purged with nitrogen (50 mL/min) and the combustor feed stream is introduced again. No blow-off or extinction is observed in the methane combustor under the investigated conditions.

According to Mundhawa et al.,[41] the combustion reaction completes in the first 20 – 30% of the channel length of the plate reactor. As the combustion reaction is much faster than the reforming reaction, heat generation overcomes the heat consumption and sudden rise in temperature is observed especially as the reaction zone do not overlap. Another possible reason for flashback in counter-current mode is the light-off phenomena through convective feedback of heat, something that is prevented in the concurrent mode.[107] To overcome sharp temperature rise in counter-current mode, a distributed feed design at multiple locations can be implemented at the cost of complex reactor design.[54, 105] The flashbacks of counter-current mode

can be avoided successfully by adjusting the flow rate, see in additional coupling experiments in Supporting Information (Figure S11 –S14).

The thermal energy input to the combustion section is about three times lower for counter-current operation due to preheating as compared to co-current operation, specifically evaluated at a furnace temperature of 730 °C. The counter-current operation benefits from heat recovery from the hot products to preheat the cold reformer feed–stream. However, this results in large temperature gradients in the reactor,[36] leading to hot spot formation. Large temperature transients and thermal gradients may also be generated during the startup.[108] Hot spots lead to higher thermal stress in the reactor in counter-current mode compared to the co-current mode.[109]

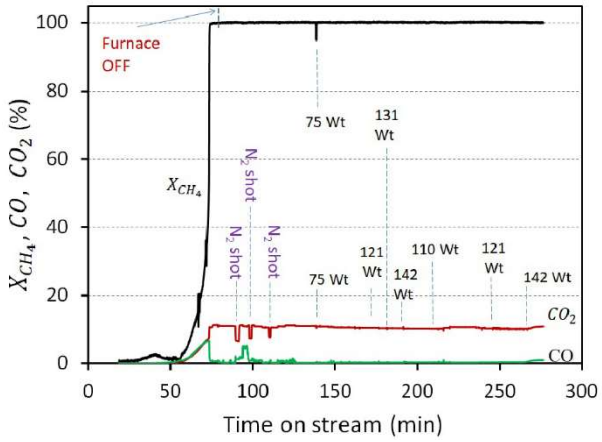


Figure 14. $CH_4$ conversion and percent of products of the combustion stream in counter-current operation as a function of time on stream.

For counter-current mode, the methane conversion and profiles of CO and $CO_2$ vs. TOS are shown in Figure 14. During the three flashbacks, the methane conversion remains at 100% whereas the $CO_2$ concentration drops due to purge-shots of $N_2$ in feed, and the CO concentration varies non-monotonically. Like the co-current operation, the energy input to the combustion increases when the furnace temperature drops. To confirm this phenomenon, the furnace is turned on to increase the temperature surrounding the CPR which results in drop in energy input from 142 to 110 $W_t$. This energy input is increased exponentially (Figure S10) again when the furnace is turned off and the furnace temperature declines to the same value with the same energy input to the combustion section. $T_{FURN}$ is dropped continuously after the turning off electric furnace that results in bigger difference $T_{REF}$ and $T_{COMB}$. At the end of the experiment, the temperature difference $T_{FURN} - T_{COMB}$ increases to 278.7 °C and energy input to the combustor rises to 142 $W_t$.

The concentration of carbon dioxide correlates with methane conversion and reaches a value of 10.7 vol% at 943 °C with complete methane conversion at 73.7 min of TOS, as seen in Figure 14. A similar trend is observed for the CO concentration with a maximum value of 6.5 vol%. After complete methane

conversion, CO declines sharply down to 2456 ppm. This confirms the catalytic combustion of methane in the catalytic plate reactor. A downward spike in methane conversion was observed at the same time which suggests a decline in methane conversion at every flow rate change during the experiment but with a quick recovery in conversion. Like co-current mode, NO is also not detected in the combustor outlet stream. The formation of $N_2O$ is confirmed at $T_{COMB}$ of 384 °C, as shown in Figure 15. During ignition, the $N_2O$ concentration increases up to 142.8 ppm with a subsequent sudden drop that remains < 9 ppm except during flashbacks and instantaneous spikes at flow variation points representing changes in energy input.

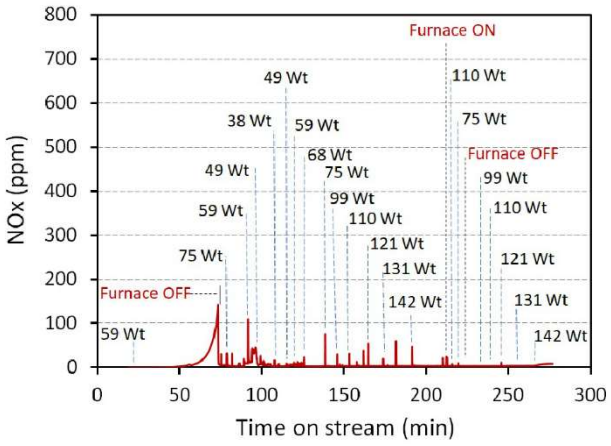


Figure 15. Concentration of $N_2O$ (ppm) for counter-current mode in the catalytic plate reactor.

For MSR in counter-current mode, the highest value of $CH_4$ conversion of 80.2% occurs at $T_{REF}$ = 1027 ºC along with CO selectivity and $H_2$ fraction of 60.4% and 70.2%, respectively (Figure 16). After switching furnace off, the $CH_4$ conversion in the reforming side drops due to heat losses. To confirm the influence of the surrounding temperature on heat losses and reactor performance, $T_{FURN}$ was increased from 704.9 ºC to 810 ºC by switching it on/off. As a result, the heat input to the combustion section decreased and the $CH_4$ conversion increased. As the difference between the furnace and CPR temperatures increased, reactor performance dropped in all cases due to external heat losses. $CH_4$ catalytic combustion reaction was self-sustained for all conditions investigated while the $CH_4$ conversion in the reforming section dropped after switching the furnace off. Ineffective insulations are the primary cause of heat losses and the small throughput of the system is not capable of keeping up. In reality, ineffective insulations were needed to initiate methane catalytic oxidation reaction by providing heat from the furnace. CPR was made of moderately conductive stainless steel wall which is also unstable under laboratory heat loss conditions.[48, 51] The increase in the number of plates in the form of a stack can help to improve stability. As in the study of Mettler et al.,[48] plate reactor stack consisting of 9 alternating steam reforming and combustion plates provides a middle ground in terms of stability.

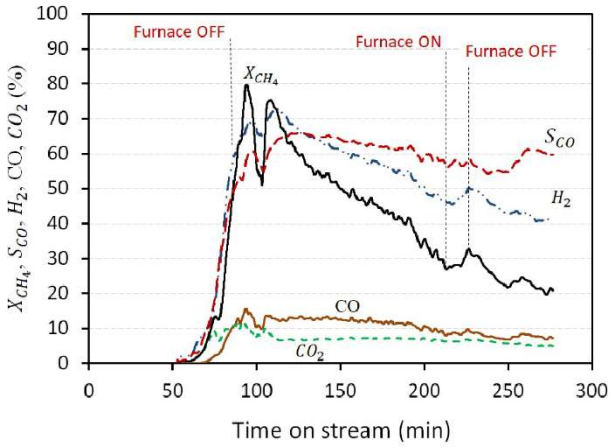


Figure 16. $CH_4$ conversion, CO selectivity and fraction of CO, $CO_2$ and $H_2$ in MSR for counter-current flow mode with methane flow rate of 45 mL/min and S/C molar ratio of 4.0.

## 4. Conclusions

With the resurged interest in distributed hydrogen production, design of small, portable, more energy efficient reformers becomes important. Due to their small size, flames typically used for heating large scale reformers are impractical and catalytic combustion is the preferred heat generation approach. A catalytic plate reactor was designed and developed to study coupling of methane combustion and methane steam reforming over 5wt%Pt/$Al_2O_3$ coated microchannels and understand the start-up behaviour. The reactor setup was assessed using CFD simulations, which showed uniform velocity and pressure distribution along the microfluidic channels. The catalyst layer shows homogeneous distribution and excellent adherence. The combustor and reformer were successfully coupled experimentally in co-current and counter-current modes, and issues posed by the CPR during startup were identified. Regarding methane conversion, the transient performance of methane steam reformer is slightly better in co-current mode than counter-current mode at the cost of three fold higher energy consumption in the combustor operating at ~1000 °C. In the catalytic methane combustor, complete conversion was achieved over a wide channel velocity range (5.1 – 57.3 m/s) without NO formation, but with $N_2O$ identified in the combustor outlet. The concentration of $N_2O$ is much lower in the counter-current mode, probably due to higher energy input in the latter. Three flashbacks were encountered in counter-current mode indicating thermal imbalance as a result of delocalization and minimal coupling of reaction zones. Mitigation strategies regarding safety were discussed. This study contributes to the understanding of coupling methane combustion and reforming in a single plate reactor in transient mode during start-up. Future work will focus on the development and experimental evaluation of CPR of multiple plates coated with active catalyst suitable for each reaction.

## Supporting Information

S1. Additional details of calculation. Table S1. Operating conditions of catalytic methane combustion for co-current flow mode. Table S2. Operating conditions of catalytic methane combustion for counter-current flow mode. Table S3. Average inlet velocity in the center of channels in CPR. Figure S1 (a – I). The velocity profile in microchannels of catalytic plate reactor at channel inlet velocity from 1.4 to 57.3 m/s. Figure S2: Difference between minimum and maximum velocities (m/s) versus average channel inlet velocity. Figure S3 (a – I). The pressure profile in microchannels of catalytic plate reactor at channel inlet velocity from 1.4 to 57.3 m/s. Table S4. Pressure drop across microchannels in catalytic plate reactor. Figure S4: Channel inlet velocity as a function of time on stream (TOS) for coupling of MSR and MC. Figure S5: Energy input as a function of $\Delta T_1 = T_{COMB} - T_{FURN}$ for co-current opeation. S2. Second co-current coupling experiment – Furnace heat management. Figure S6: Temperature profile of co-current mode in CPR managed by furnace heat. Figure S7: $CH_4$ conversion, CO selectivity and percent profiles ($H_2$, CO and $CO_2$) of MSR for co-current furnace heat managed with a methane flow (45 mL/min) and S/C of 5.0 (172 NL/h/$g_{cat}$). Figure S8: Methane conversion and concentration profiles in the combustion side in co-current operation as a function of time on stream (furnace heat managed). Figure S9: The concentration of $N_2O$ (ppm) for co-current mode in CPR (furnace heat managed). Figure S10: Energy input as a function of $\Delta T_2 = T_{COMB} - T_{FURN}$ for counter-current operation. S3. Second counter-current coupling experiment. Figure S11. The temperature profile for second counter current coupling experiment. Figure S12. $CH_4$ conversion and concentration profiles of on combustion side for counter-current operation as a function of time on stream. Figure S13. The concentration of $N_2O$ (ppm) for counter-current mode in catalytic plate reactor. Figure S14. $CH_4$ conversion, CO selectivity and concentration profiles (CO, $CO_2$ and $H_2$) of methane steam reforming for counter-current flow mode with methane flow rate of 45 mL/min and S/C molar ratio of 4.0.

## Conflicts of Interest

There is no conflict of interest to declare.

## Acknowledgements

The work of DGV was supported from Department of Energy's Office of Energy Efficient and Renewable Energy's Advanced Manufacturing Office under Award Number DE-EE0007888-8.3. The Delaware Energy Institute gratefully acknowledges the support and partnership of the State of Delaware toward the RAPID projects.

## References

1. Staffell, I.; Scamman, D.; Velazquez Abad, A.; Balcombe, P.; Dodds, P. E.; Ekins, P.; Shah, N.; Ward, K. R., The role of hydrogen and fuel cells in the global energy system. *Energy & Environmental Science* **2019,** 12, (2), 463-491.

2. Züttel, A.; Borgschulte, A.; Schlapbach, L., *Hydrogen as a Future Energy Carrier*. Wiley-VCH Verlag GmbH & Co. KGaA: Weinheim, 2008.

3. Wilhite, B. A., Unconventional microreactor designs for process intensification in the distributed reforming of hydrocarbons: a review of recent developments at Texas A&M University. *Current Opinion in Chemical Engineering* **2017,** 17, 100-107.

4. Southall, G. D.; Khare, A., The feasibility of distributed hydrogen production from renewable energy sources and the financial contribution from UK motorists on environmental grounds. *Sustainable Cities and Society* **2016,** 26, 134-149.

5. Bolat, P.; Thiel, C., Hydrogen supply chain architecture for bottom-up energy systems models. Part 2: Techno-economic inputs for hydrogen production pathways. *Int J Hydrogen Energ* **2014,** 39, (17), 8898-8925.

6. Ercolino, G.; Ashraf, M. A.; Specchia, V.; Specchia, S. In *Performance of SR or ATR fuel processors integrated with WGS and PSA units for hydrogen production*, Roma, 2014; Roma, 2014; pp 232-233.

7. Ashraf, M. A.; Ercolino, G.; Specchia, S.; Specchia, V., Final step for CO syngas clean-up: Comparison between CO-PROX and CO-SMET processes. *Int J Hydrogen Energ* **2014,** 39, (31), 18109-18119.

8. Gandia, L. M.; Arzamedi, G.; Dieguez, P. M., *Renewable Hydrogen Technologies: Production, Purification, Storage, Applications and Safety*. Elsevier: Amsterdam, 2013; p 472.

9. Vita, A.; Cristiano, G.; Italiano, C.; Pino, L.; Specchia, S., Syngas production by methane Oxy-steam reforming on Me/CeO2 (Me = Rh, Pt, Ni) catalyst lined on cordierite monoliths. *Appl Catal B-Environ* **2015,** 162, 551-563.

10. Gupta, R. B., *Hydrogen Fuel: Production, Transport, and Storage*. CRC Press, Taylor & Francis Group: Boca Raton, 2009.

11. Sanz, O.; Echave, F. J.; Romero-Sarria, F.; Odriozola, J. A.; Montes, M., Chapter 9 - Advances in Structured and Microstructured Catalytic Reactors for Hydrogen Production. In *Renewable Hydrogen Technologies*, Gandía, L. M.; Arzamendi, G.; Diéguez, P. M., Eds. Elsevier: Amsterdam, 2013; pp 201-224.

12. Adris, A. M.; Pruden, B. B.; Lim, C. J.; Grace, J. R., On the reported attempts to radically improve the performance of the steam methane reforming reactor. *The Canadian Journal of Chemical Engineering* **1996,** 74, (2), 177-186.

13. Kumar, A.; Baldea, M.; Edgar, T. F., A physics-based model for industrial steam-methane reformer optimization with non-uniform temperature field. *Computers & Chemical Engineering* **2017,** 105, 224-236.

14. Kumar, A.; Baldea, M.; Edgar, T. F., Real-time optimization of an industrial steam-methane reformer under distributed sensing. *Control Engineering Practice* **2016,** 54, 140-153.

15. Zecevic, N.; Bolf, N., Advanced Operation of the Steam Methane Reformer by Using Gain-Scheduled Model Predictive Control. *Ind Eng Chem Res* **2020,** 59, (8), 3458-3474.

16. Oechsler, B. F.; Dutra, J. C. S.; Bittencourt, R. C. P.; Pinto, J. C., Simulation and Control of Steam Reforming of Natural Gas—Reactor Temperature Control Using Residual Gas. *Ind Eng Chem Res* **2017,** 56, (10), 2690-2710.

17. Weinberg, F. J., Combustion Temperatures: The Future? *Nature* **1971,** 233, (5317), 239-241.

18. Hayes, R. E.; Kolaczkowski, S. T., *Introduction to catalytic combustion*. Gordon & Breach Science Publishers: Amsterdam, 1997.

19. Pfefferle, W. C.; Pfefferle, L. D., Catalytically stabilized combustion. *Progress in Energy and Combustion Science* **1986,** 12, (1), 25-41.

20. Coker, A. K., *Petroleum Refining Design and Applications Handbook*. John Wiley & Sons: USA, 2018; Vol. Volume 1.

21. Kolb, G., Review: Microstructured reactors for distributed and renewable production of fuels and electrical energy. *Chemical Engineering and Processing: Process Intensification* **2013,** 65, 1-44.

22. Colorado, A.; McDonell, V.; Samuelsen, S., Direct emissions of nitrous oxide from combustion of gaseous fuels. *Int J Hydrogen Energ* **2017,** 42, (1), 711-719.

23. Karagiannidis, S., *Catalytic Microreactors for Portable Power Generation*. Springer-Verlag: Heidelberg, 2011.

24. He, L.; Fan, Y.; Bellettre, J.; Yue, J.; Luo, L., A review on catalytic methane combustion at low temperatures: Catalysts, mechanisms, reaction conditions and reactor designs. *Renewable and Sustainable Energy Reviews* **2020,** 119, 109589.

25. Kolios, G.; Gritsch, A.; Glöckler, B.; Eigenberger, G., Enhancing Productivity and Thermal Efficiency of High-Temperature Endothermic Processes in Heat-Integrated Fixed-Bed Reactors. In *Integrated Chemical Processes*, Sundmacher, K.; Kienle, A.; Seidel-Morgenstern, A., Eds. WILEY-VCH Verlag GmbH & Co. KGaA: Weinheim, 2005; pp 1-43.

26. Meloni, E.; Martino, M.; Palma, V., A Short Review on Ni Based Catalysts and Related Engineering Issues for Methane Steam Reforming. *Catalysts* **2020,** 10, (3).

27. Luk, H. T.; Lei, H. M.; Ng, W. Y.; Ju, Y.; Lam, K. F., Techno-economic Analysis of Distributed Hydrogen Production from Natural Gas. *Chinese J Chem Eng* **2012,** 20, (3), 489-496.

668 28. Stefanidis, G. D.; Vlachos, D. G., Millisecond Methane Steam Reforming Via Process and
669 Catalyst Intensification. *Chem Eng Technol* **2008,** 31, (8), 1201-1209.
670 29. Chen, J.; Gao, X.; Xu, D., Catalytic Combustion Characteristics of Methane-Air Mixtures in
671 Small-Scale Systems at Elevated Temperatures. *Catalysts* **2018,** 8, (10), 439.
672 30. Venkataraman, K.; Redenius, J. M.; Schmidt, L. D., Millisecond catalytic wall reactors:
673 dehydrogenation of ethane. *Chem Eng Sci* **2002,** 57, (13), 2335-2343.
674 31. Venkataraman, K.; Wanat, E. C.; Schmidt, L. D., Steam reforming of methane and water-gas
675 shift in catalytic wall reactors. *Aiche J* **2003,** 49, (5), 1277-1284.
676 32. Kolb, G.; Schürer, J.; Tiemann, D.; Wichert, M.; Zapf, R.; Hessel, V.; Löwe, H., Fuel processing
677 in integrated micro-structured heat-exchanger reactors. *J Power Sources* **2007,** 171, (1), 198-204.
678 33. Specchia, S., Fuel processing activities at European level: A panoramic overview. *Int J Hydrogen*
679 *Energ* **2014,** 39, (31), 17953-17968.
680 34. Dodds, P. E.; Staffell, I.; Hawkes, A. D.; Li, F.; Grünewald, P.; McDowall, W.; Ekins, P.,
681 Hydrogen and fuel cell technologies for heating: A review. *Int J Hydrogen Energ* **2015,** 40, (5), 2065-
682 2083.
683 35. Specchia, S.; Specchia, V., Modeling Study on the Performance of an Integrated APU Fed with
684 Hydrocarbon Fuels. *Ind Eng Chem Res* **2010,** 49, (15), 6803-6809.
685 36. Zanfir, M.; Gavriilidis, A., Catalytic combustion assisted methane steam reforming in a catalytic
686 plate reactor. *Chem Eng Sci* **2003,** 58, (17), 3947-3960.
687 37. Chen, J.; Han, J.; Xu, D., Efficient operation of autothermal microchannel reactors for the
688 production of hydrogen by steam methane reforming. *Int J Hydrogen Energ* **2019,** 44, (23), 11546-11563.
689 38. Mundhwa, M.; Thurgood, C. P., Improved performance of a catalytic plate reactor coated with
690 distributed layers of reforming and combustion catalysts for hydrogen production. *Reaction Chemistry &*
691 *Engineering* **2018,** 3, (4), 487-514.
692 39. Chen, J.; Gao, X.; Yan, L.; Xu, D., Computational fluid dynamics modeling of the millisecond
693 methane steam reforming in microchannel reactors for hydrogen production. *Rsc Adv* **2018,** 8, (44),
694 25183-25200.
695 40. Mundhwa, M.; Thurgood, C. P., Numerical study of methane steam reforming and methane
696 combustion over the segmented and continuously coated layers of catalysts in a plate reactor. *Fuel*
697 *Process Technol* **2017,** 158, 57-72.
698 41. Mundhwa, M.; Parmar, R. D.; Thurgood, C. P., A comparative parametric study of a catalytic
699 plate methane reformer coated with segmented and continuous layers of combustion catalyst for
700 hydrogen production. *J Power Sources* **2017,** 344, 85-102.

42. Chen, J.; Yan, L.; Song, W.; Xu, D., Methane steam reforming thermally coupled with catalytic combustion in catalytic microreactors for hydrogen production. *Int J Hydrogen Energ* **2017,** 42, (1), 664-680.
43. Cao, C.; Zhang, N.; Dang, D.; Cheng, Y., Numerical evaluation of a microchannel methane reformer used for miniaturized GTL: Operating characteristics and greenhouse gases emission. *Fuel Process Technol* **2017,** 167, 78-91.
44. Cao, C.; Zhang, N.; Dang, D.; Cheng, Y., Hybrid modeling of integrated microchannel methane reformer for miniaturized GTL application using an effectiveness factor submodel based on complex surface chemistry. *Chem Eng J* **2017,** 316, 715-726.
45. Cao, C.; Zhang, N.; Cheng, Y., Numerical analysis on steam methane reforming in a plate microchannel reactor: Effect of washcoat properties. *Int J Hydrogen Energ* **2016,** 41, (42), 18921-18941.
46. Lakhete, P.; Janardhanan, V. M., Modeling process intensified catalytic plate reactor for synthesis gas production. *Chem Eng Sci* **2014,** 110, 13-19.
47. Jeon, S. W.; Yoon, W. J.; Baek, C.; Kim, Y., Minimization of hot spot in a microchannel reactor for steam reforming of methane with the stripe combustion catalyst layer. *Int J Hydrogen Energ* **2013,** 38, (32), 13982-13990.
48. Mettler, M. S.; Stefanidis, G. D.; Vlachos, D. G., Enhancing stability in parallel plate microreactor stacks for syngas production. *Chem Eng Sci* **2011,** 66, (6), 1051-1059.
49. Zhai, X.; Ding, S.; Cheng, Y.; Jin, Y.; Cheng, Y., CFD simulation with detailed chemistry of steam reforming of methane for hydrogen production in an integrated micro-reactor. *Int J Hydrogen Energ* **2010,** 35, (11), 5383-5392.
50. Stefanidis, G. D.; Vlachos, D. G., Intensification of steam reforming of natural gas: Choosing combustible fuel and reforming catalyst. *Chem Eng Sci* **2010,** 65, (1), 398-404.
51. Mettler, M. S.; Stefanidis, G. D.; Vlachos, D. G., Scale-out of Microreactor Stacks for Portable and Distributed Processing: Coupling of Exothermic and Endothermic Processes for Syngas Production. *Ind Eng Chem Res* **2010,** 49, (21), 10942-10955.
52. Tonkovich, A. L. Y.; Yang, B.; Perry, S. T.; Fitzgerald, S. P.; Wang, Y., From seconds to milliseconds to microseconds through tailored microchannel reactor design of a steam methane reformer. *Catal Today* **2007,** 120, (1), 21-29.
53. Zanfir, M.; Gavriilidis, A., Influence of Flow Arrangement in Catalytic Plate Reactors for Methane Steam Reforming. *Chemical Engineering Research and Design* **2004,** 82, (2), 252-258.
54. Kolios, G.; Frauhammer, J.; Eigenberger, G., Efficient reactor concepts for coupling of endothermic and exothermic reactions. *Chem Eng Sci* **2002,** 57, (9), 1505-1510.

734 55. Nikačević, N. M.; Huesman, A. E. M.; Van den Hof, P. M. J.; Stankiewicz, A. I., Opportunities
735 and challenges for process control in process intensification. *Chemical Engineering and Processing:*
736 *Process Intensification* **2012,** 52, 1-15.
737 56. Pattison, R. C.; Estep, F. E.; Baldea, M., Pseudodistributed Feed Configurations for Catalytic
738 Plate Microchannel Reactors. *Ind Eng Chem Res* **2014,** 53, (13), 5028-5037.
739 57. Ohi, T.; Miyata, T.; Li, D.; Shishido, T.; Kawabata, T.; Sano, T.; Takehira, K., Sustainability of
740 Ni loaded Mg–Al mixed oxide catalyst in daily startup and shutdown operations of CH4 steam reforming.
741 *Applied Catalysis A: General* **2006,** 308, 194-203.
742 58. Granlund, M. Z.; Gorke, O.; Pfeifer, P.; Pettersson, L. J., Comparison between a micro reactor
743 with multiple air inlets and a monolith reactor for oxidative steam reforming of diesel. *Int J Hydrogen*
744 *Energ* **2014,** 39, (31), 18037-18045.
745 59. Zanfir, M.; Baldea, M.; Daoutidis, P., Optimizing the catalyst distribution for countercurrent
746 methane steam reforming in plate reactors. *Aiche J* **2011,** 57, (9), 2518-2528.
747 60. Jeon, S. W.; Yoon, W. J.; Jeong, M. W.; Kim, Y., Optimization of a counter-flow microchannel
748 reactor using hydrogen assisted catalytic combustion for steam reforming of methane. *Int J Hydrogen*
749 *Energ* **2014,** 39, (12), 6470-6478.
750 61. Herdem, M. S.; Mundhwa, M.; Farhad, S.; Hamdullahpur, F., Catalyst layer design and
751 arrangement to improve the performance of a microchannel methanol steam reformer. *Energ Convers*
752 *Manage* **2019,** 180, 149-161.
753 62. Pattison, R. C.; Baldea, M., A thermal-flywheel approach to distributed temperature control in
754 microchannel reactors. *Aiche J* **2013,** 59, (6), 2051-2061.
755 63. Pattison, R. C.; Donahue, M. M.; Gupta, A. M.; Baldea, M., Localized Temperature Control in
756 Microchannel Reactors Using Bimetallic Thermally-Actuated Valves. *Ind Eng Chem Res* **2015,** 54, (24),
757 6355-6361.
758 64. Welty, J.; Rorrer, G. L.; Foster, D. G., *Fundamentals of Momentum, Heat, and Mass Transfer*.
759 7th ed.; John Wiley & Sons: Hoboken, NJ,, 2019; p 784.
760 65. Tonkovich, A. Y.; Perry, S.; Wang, Y.; Qiu, D.; LaPlante, T.; Rogers, W. A., Microchannel
761 process technology for compact methane steam reforming. *Chem Eng Sci* **2004,** 59, (22-23), 4819-4824.
762 66. Irankhah, A.; Rahimi, M.; Rezaei, M., Performance Research on a Methane Compact Reformer
763 Integrated with Catalytic Combustion. *Chem Eng Technol* **2014,** 37, (7), 1220-1226.
764 67. Commenge, J. M.; Falk, L.; Corriou, J. P.; Matlosz, M., Optimal design for flow uniformity in
765 microchannel reactors. *Aiche J* **2002,** 48, (2), 345-358.

68. Stefanidis, G. D.; Vlachos, D. G.; Kaisare, N. S.; Maestri, M., Methane steam reforming at microscales: Operation strategies for variable power output at millisecond contact times. *Aiche J* **2009,** 55, (1), 180-191.

69. Farrauto, R. J., New catalysts and reactor designs for the hydrogen economy. *Chem Eng J* **2014,** 238, 172-177.

70. Ashraf, M. A.; Sanz, O.; Italiano, C.; Vita, A.; Montes, M.; Specchia, S., Analysis of Ru/La-Al2O3 catalyst loading on alumina monoliths and controlling regimes in methane steam reforming. *Chem Eng J* **2018,** 334, 1792-1807.

71. Ashraf, M. A.; Sanz, O.; Montes, M.; Specchia, S., Insights into the effect of catalyst loading on methane steam reforming and controlling regime for metallic catalytic monoliths. *Int J Hydrogen Energ* **2018,** 43, (26), 11778-11792.

72. Amjad, U.-E. S.; Vita, A.; Galletti, C.; Pino, L.; Specchia, S., Comparative Study on Steam and Oxidative Steam Reforming of Methane with Noble Metal Catalysts. *Ind Eng Chem Res* **2013,** 52, (44), 15428-15436.

73. Ercolino, G.; Stelmachowski, P.; Specchia, S., Catalytic Performance of Pd/Co3O4 on SiC and ZrO2 Open Cell Foams for Process Intensification of Methane Combustion in Lean Conditions. *Ind Eng Chem Res* **2017,** 56, (23), 6625-6636.

74. Tacchino, S.; Vella, L. D.; Specchia, S., Catalytic combustion of CH4 and H2 into micro-monoliths. *Catal Today* **2010,** 157, (1), 440-445.

75. Otto, K., Methane oxidation over Pt on γ-alumina: kinetics and structure sensitivity. *Langmuir* **1989,** 5, (6), 1364-1369.

76. Peela, N. R.; Mubayi, A.; Kunzru, D., Washcoating of γ-alumina on stainless steel microchannels. *Catal Today* **2009,** 147, S17-S23.

77. Zhang, Q.; Sakurai, M.; Kameyama, H., Performance Simulations of a Compact Plate Methane Steam Reformer Using an Electrically Heated Alumite Catalyst. *Journal of Chemical Engineering of Japan* **2007,** 40, (4), 319-328.

78. Haruta, M.; Sano, H., Catalytic combustion of hydrogen—III. Advantages and disadvantages of a catalytic heater with hydrogen fuel. *Int J Hydrogen Energ* **1982,** 7, (9), 737-740.

79. Maximini, M.; Engelhardt, P.; Brenner, M.; Beckmann, F.; Moritz, O., Fast start-up of a diesel fuel processor for PEM fuel cells. *Int J Hydrogen Energ* **2014,** 39, (31), 18154-18163.

80. Chen, F.; Chang, M.-H.; Kuo, C.-Y.; Hsueh, C.-Y.; Yan, W.-M., Analysis of a Plate-Type Microreformer for Methanol Steam Reforming Reaction. *Energy & Fuels* **2009,** 23, (10), 5092-5098.

81. Rodríguez-Guerra, Y.; Gerling, L. A.; López-Guajardo, E. A.; Lozano-García, F. J.; Nigam, K. D. P.; Montesinos-Castellanos, A., Design of Micro- and Milli-Channel Heat Exchanger Reactors for

800 Homogeneous Exothermic Reactions in the Laminar Regime. *Ind Eng Chem Res* **2016,** 55, (22), 6435-
801 6442.
802 82. Ahmed, K.; Föger, K., Fuel Processing for High-Temperature High-Efficiency Fuel Cells. *Ind*
803 *Eng Chem Res* **2010,** 49, (16), 7239-7256.
804 83. Janicke, M. T.; Kestenbaum, H.; Hagendorf, U.; Schüth, F.; Fichtner, M.; Schubert, K., The
805 Controlled Oxidation of Hydrogen from an Explosive Mixture of Gases Using a Microstructured
806 Reactor/Heat Exchanger and Pt/Al2O3 Catalyst. *J Catal* **2000,** 191, (2), 282-293.
807 84. Ryi, S. K.; Park, J. S.; Cho, S. H.; Kim, S. H., Fast start-up of microchannel fuel processor
808 integrated with an igniter for hydrogen combustion. *J Power Sources* **2006,** 161, (2), 1234-1240.
809 85. Yang, J.; Salman, A. D.; Blanco-García, P., A Review of Measurement Techniques of
810 Mechanical Properties of the Catalyst Layer in Catalytic Converters. *Johnson Matthey Technology*
811 *Review* **2019,** 63, (3), 177-190.
812 86. Vican, J.; Gajdeczko, B. F.; Dryer, F. L.; Milius, D. L.; Aksay, I. A.; Yetter, R. A., Development
813 of a microreactor as a thermal source for microelectromechanical systems power generation. *Proceedings*
814 *of the Combustion Institute* **2002,** 29, (1), 909-916.
815 87. Belmont, E. L.; Schoegl, I.; Ellzey, J. L., Experimental and analytical investigation of lean
816 premixed methane/air combustion in a mesoscale counter-flow reactor. *Proceedings of the Combustion*
817 *Institute* **2013,** 34, (2), 3361-3367.
818 88. He, L.; Fan, Y.; Luo, L.; Bellettre, J.; Yue, J., Preparation of Pt/γ-Al2O3 catalyst coating in
819 microreactors for catalytic methane combustion. *Chem Eng J* **2020,** 380, 122424.
820 89. Zanfir, M.; Gavriilidis, A., Modelling of a catalytic plate reactor for dehydrogenation–
821 combustion coupling. *Chem Eng Sci* **2001,** 56, (8), 2671-2683.
822 90. Lee, J. H.; Trimm, D. L., Catalytic combustion of methane. *Fuel Process Technol* **1995,** 42, (2),
823 339-359.
824 91. Chen, J.; Gao, X.; Liu, B.; Xu, D., Management of the gas-phase and surface chemistry in
825 methane-fueled catalytic micro-combustors. *Int J Hydrogen Energ* **2017,** 42, (30), 19079-19095.
826 92. Wang, Y.; Yang, W.; Zhou, J.; Yang, H.; Yao, Y.; Cen, K., Heterogeneous reaction
827 characteristics and its effects on homogeneous combustion of methane/air mixture in microchannels II.
828 Chemical analysis. *Fuel* **2019,** 235, 923-932.
829 93. Robinson, C.; Smith, D. B., The auto-ignition temperature of methane. *Journal of Hazardous*
830 *Materials* **1984,** 8, (3), 199-203.
831 94. Farrauto, R. J.; Liu, Y.; Ruettinger, W.; Ilinich, O.; Shore, L.; Giroux, T., Precious Metal
832 Catalysts Supported on Ceramic and Metal Monolithic Structures for the Hydrogen Economy. *Catalysis*
833 *Reviews* **2007,** 49, (2), 141-196.

95. Boldrini, D. E.; Sanchez, J. F.; Tonetto, G. M.; Damiani, D. E., Monolithic Stirrer Reactor: Performance in the Partial Hydrogenation of Sunflower Oil. *Ind Eng Chem Res* **2012,** 51, (38), 12222-12232.

96. Ertl, G.; Knözinger, H.; Weitkamp, J., *Handbook of heterogeneous catalysis*. VCH Verlagsgesellschaft mbH: Weinheim, 1997.

97. Ismagilov, Z. R.; Pushkarev, V. V.; Podyacheva, O. Y.; Koryabkina, N. A.; Veringa, H., A catalytic heat-exchanging tubular reactor for combining of high temperature exothermic and endothermic reactions. *Chem Eng J* **2001,** 82, (1-3), 355-360.

98. Baukal, C. E., *The John Zink Hamworthy Combustion Handbook: Fundamentals*. CRC Press: Danvers, MA, 2013; Vol. Vol. 1.

99. Bowman, C. T., Gas-Phase Reaction Mechanisms for Nitrogen Oxide Formation and Removal in Combustion. In *Pollutants from Combustion: Formation and Impact on Atmospheric Chemistry*, Vovelle, C., Ed. Springer: Dordrecht, 2000; pp 123-144.

100. Muzio, L. J.; Montgomery, T. A.; Samuelsen, G. S.; Kramlich, J. C.; Lyon, R. K.; Kokkinos, A., Formation and measurement of N2O in combustion systems. *Symposium (International) on Combustion* **1991,** 23, (1), 245-250.

101. Kumar, A.; Baldea, M.; Edgar, T. F.; Ezekoye, O. A., Smart Manufacturing Approach for Efficient Operation of Industrial Steam-Methane Reformers. *Ind Eng Chem Res* **2015,** 54, (16), 4360-4370.

102. Glarborg, P.; Miller, J. A.; Ruscic, B.; Klippenstein, S. J., Modeling nitrogen chemistry in combustion. *Progress in Energy and Combustion Science* **2018,** 67, 31-68.

103. Wójcik, S.; Ercolino, G.; Gajewska, M.; Quintero, C. W. M.; Specchia, S.; Kotarba, A., Robust Co3O4|α-Al2O3|cordierite structured catalyst for N2O abatement – Validation of the SCS method for active phase synthesis and deposition. *Chem Eng J* **2019,** 377, 120088.

104. Hayhurst, A. N.; Lawrence, A. D., Emissions of nitrous oxide from combustion sources. *Progress in Energy and Combustion Science* **1992,** 18, (6), 529-552.

105. Kolios, G.; Glockler, B.; Gritsch, A.; Morillo, A.; Eigenberger, G., Heat-integrated reactor concepts for hydrogen production by methane steam reforming. *Fuel Cells* **2005,** 5, (1), 52-65.

106. Plee, S. L.; Mellor, A. M., Review of flashback reported in prevaporizing/premixing combustors. *Combustion and Flame* **1978,** 32, 193-203.

107. Kolios, G.; Frauhammer, J.; Eigenberger, G., A simplified procedure for the optimal design of autothermal reactors for endothermic high-temperature reactions. *Chem Eng Sci* **2001,** 56, (2), 351-357.

108. Dhingra, A. Modeling and Development of Compact Onboard Fuel Processors for PEM Fuel Cell Applications. The University of Michigan, USA, 2012.

868 109. Frauhammer, J.; Eigenberger, G.; Hippel, L. v.; Arntz, D., A new reactor concept for
869 endothermic high-temperature reactions. *Chem Eng Sci* **1999,** 54, (15), 3661-3670.

870

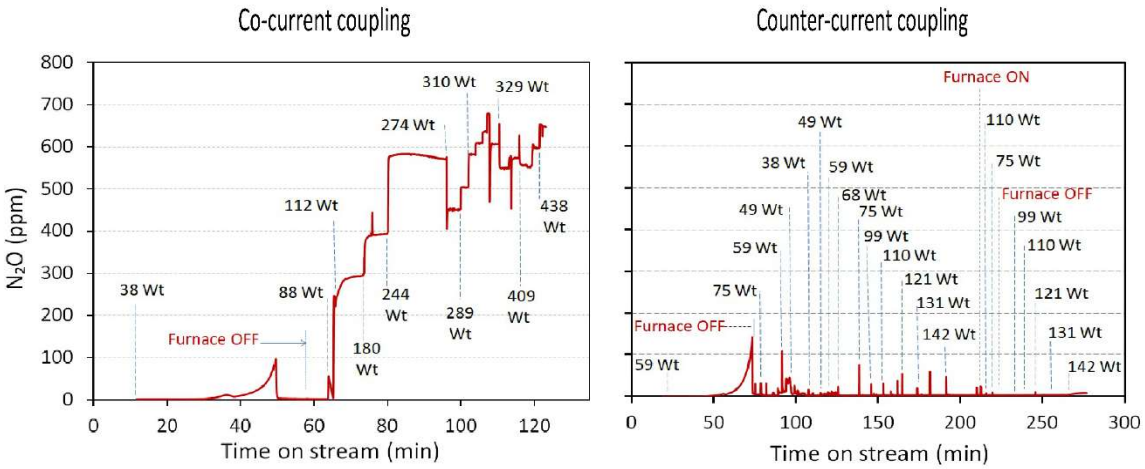
Co-current coupling
N2O (ppm)
Time on stream (min)
38 Wt
88 Wt
112 Wt
180 Wt
244 Wt
274 Wt
289 Wt
310 Wt
329 Wt
409 Wt
438 Wt
Furnace OFF
Counter-current coupling
Time on stream (min)
Furnace ON
Furnace OFF
49 Wt
38 Wt
59 Wt
68 Wt
75 Wt
99 Wt
110 Wt
121 Wt
131 Wt
142 Wt

871